

Boxx, M. Stöhr, C. Carter and W. Meier, Sustained multi-kHz flamefront and 3-component velocity-field measurements for the study of turbulent flames. *Applied Physics B* 95 (1), 23-29 (2009).

The original publication is available at [www.springerlink.com](http://www.springerlink.com)

<http://dx.doi.org/10.1007/s00340-009-3420-4>

DRAFT  
Applied Physics B – Rapid Communication

**Sustained multi-kHz flamefront and 3-component velocity-field  
measurements for the study of turbulent flames**

I. Boxx<sup>1</sup>, M. Stöhr<sup>1</sup>, C. Carter<sup>2</sup>, W. Meier<sup>1</sup>

1: Institut für Verbrennungstechnik, Deutsches Zentrum für Luft-und Raumfahrt (DLR),  
Pfaffenwaldring 38-40, D-70569 Stuttgart, Germany

2: Air Force Research Laboratory (AFRL) / RZAS  
1950 Fifth St, Wright-Patterson AFB, OH USA

**Corresponding Author:** Isaac Boxx, Pfaffenwaldring 38-40, D-70569 Stuttgart,  
Germany, Fax: (+49) 711 6862 578, e-mail: [Isaac.Boxx@dlr.de](mailto:Isaac.Boxx@dlr.de)

**Abstract**

We describe an approach of imaging the dynamic interaction of the flamefront and flowfield. Here, a diode- pumped Nd:YLF laser operating at 5 kHz is used to pump a dye laser, which is then frequency doubled to 283 nm to probe flamefront OH, while a dual cavity diode-pumped Nd:YAG system produces pulse-pairs for particle image velocimetry (PIV). CMOS digital cameras are used to detect both planar laser-induced fluorescence (PLIF) and particle scattering (in a stereo arrangement) such that a 5 kHz measurement frequency is attained. This diagnostic is demonstrated in lifted-jet and swirl-stabilized flames, wherein the dynamics of the flame stabilization processes are seen. Non-periodic effects such as local ignition and/or extinction, lift-off and flashback events and their histories can be captured by this technique. As such, this system has the potential to significantly extend our understanding of nonstationary combustion processes relevant to industrial and technical applications.

## Introduction

The laser-based diagnostic *particle image velocimetry*, PIV, particularly that approach based on digital recording of the image, has revolutionized experimental fluid dynamics. In PIV [1] two images of a particle-laden flowfield, each illuminated by a laser sheet (with timing difference of  $\Delta t$  between the two laser pulses), are recorded, typically with an interline-transfer, charge-coupled device, CCD, camera. The two images are then divided into sub-regions, and cross correlations are performed on the sub-regions to determine the displacement vector,  $\Delta \bar{x}$ , of the group of particles within each sub-region (or interrogation region) from the first image to the second image; thus, an in-plane velocity vector is given by  $\Delta \bar{v} = \Delta \bar{x} / \Delta t$ . Furthermore, with a stereoscopic implementation using two cameras, the out-of-plane displacement, and thus velocity, can be determined. Additional quantities such as vorticity, strain, dilatation, etc., can also be derived. The combination of planar laser-induced fluorescence (PLIF) and PIV has proven to be a very powerful diagnostic tool for study of turbulent flowfields, particularly reacting ones. Development of this diagnostic began only about 12 years ago. Frank et al. [2] describe the first implementation of this combined diagnostic using PLIF of biacetyl, used as a fuel tracer. The first application of combined PIV/PLIF using a flamefront marker (OH) is described by Hasselbrink et al. [3].

These studies have employed conventional flash-lamp-pumped, Q-switched Nd:YAG lasers that typically operate at 10 Hz pulse repetition frequency. Thus, for both PIV and PLIF, the framing rate is limited to 10 frames/s, fps, and flowfield structures in consecutive images are typically uncorrelated. However, for several years now, researchers have applied lasers and digital cameras capable of acquiring image data at kHz frequencies. This is most easily done for

PIV, since one can use the frequency-doubled output of an Nd-based laser. This type of laser is typically pumped by a diode bar(s), rather than flashlamps, allowing operation at kHz repetition frequencies. The digital cameras, which can be either intensified (using a micro-channel plate, MCP) or un-intensified, are based on CMOS chips rather than CCD chips. The number of frames that can be recorded is limited by the RAM available within the camera, and a record length of 1000 images or more is readily attainable. Using diode-bar-pumped lasers and CMOS cameras, it is thus possible to image at kHz rates scalar and velocity fields; this has been demonstrated for free jet by Fajardo, et al. [4]. Here, they used a frequency-tripled Nd:YAG laser, triggered at 12 kHz, for simultaneous biacetyl PLIF and PIV.

Although the PIV-seed particle boundary can be an adequate flamefront marker, see Steinberg et al. [6] and Upatnieks et al. [5], it is nonetheless desirable to track the flamefront using a radical, such as OH or CH, that is generated at the flamefront. One approach to designing a high-speed PLIF system is to use multiple flash-lamp-pumped Nd:YAG lasers [7,8]. While this offers much flexibility in terms of timing and pulse energy, only a small number of frames can be recorded (e.g., eight), limited primarily by the number of lasers that one can reasonably assemble. Other approaches are possible too, for example using so-called pulse-burst laser systems [9,10]; this is well suited for very high-speed imaging (e.g., at rates as high as 1 MHz), and recently it has been demonstrated for OH PLIF imaging of a H<sub>2</sub>-air jet flame at rates of 50 kHz for a sequence of 20 frames. While Paa et al. [11] have reported OH PLIF imaging at 1 kHz using a tunable, frequency-tripled Yb:YAG disk laser, pumping a transition in the  $A^2\Sigma^+ - X^2\Pi$  ( $v'=0, v''=1$ ) band of OH, Wäsle et al. [12], Kittler et al. [13] and Boxx et al. [14,15] have shown that kHz pumping of a *conventional* dye laser, equipped with high-flowrate dye pump, is also possible.

The purpose of this paper is to describe a combined kHz-framing PIV-PLIF system similar to the one described by Boxx et al [14-15]. However, this combined PLIF-PIV system is different in some respects and has been allowed to mature as well. First, the system described herein operates at 5 kHz vs. 1.5 kHz. Second, some improvements have been made in the PLIF system that allow better image quality even at the higher framing/repetition rate, and indeed the OH image quality is good by any standard. The PIV system has been configured to work at this higher framing rate and still achieve a reasonable spatial resolution of  $\sim 1$  mm; a novel approach to extending the dynamic range for velocity measurements is also discussed. The capabilities of this system—for imaging three components of velocity, with stereo PIV and the OH field—are demonstrated with measurements in both lifted jet and swirl-stabilized flames. Both have unsteady flowfield/flame interactions that serve to demonstrate the remarkable utility of combined kHz PLIF and PIV.

## **Experimental Facility**

### Planar Laser-Induced Fluorescence System

The dye laser (Sirah Cobra-Stretch, with kHz modification) was pumped with a frequency-doubled, diode-pumped solid state Nd:YLF laser (Edgewave IS-811E), operating at 523 nm. At 5 kHz, the pump laser delivered 3.8 mJ/pulse (19 W average output) with 8.5 ns pulse duration. Due to the relatively low pulse energy of the pump-laser, the dye laser uses only an oscillator and pre-amplifier (in a single dye cell) and has no main amplifier. To avoid bleaching of the dye, Rhodamine 6G in methanol, at these high repetition frequencies, the laser was equipped with a high flowrate dye pump; in addition, the dye solution was cooled using a simple heat-exchanger within the dye reservoir. A BBO crystal was used for frequency doubling of the dye beam. The 566-nm dye beam was focused into a BBO crystal for efficient frequency doubling. Conversion

efficiency in this crystal ranged from 10 to 17%, depending on repetition rate (and hence the fluence of the incoming beam). Isolation of the dye and frequency-doubled beams was accomplished with a four-prism separator. At a 5 kHz pump frequency, the time-average output from the dye laser at 283.2 nm was ~0.5 W or 100  $\mu$ J/pulse. Wavelength tuning of the dye laser to the peak of the isolated Q<sub>1</sub>(7) line of the A-X (1,0) transition of OH was checked daily using a setup consisting of a laminar reference flame and a photomultiplier tube for fluorescence detection.

The 283.2 nm beam was formed into a sheet of ~40 mm (high in the probe region) using two fused silica lenses ( $f_{\text{plif1}} = -25$  mm,  $f_{\text{plif2}} = 250$  mm) in a cylindrical telescope configuration and focused to a waist using a third cylindrical lens ( $f_{\text{plif3}} = 500$  mm). The 283-nm laser sheet was overlapped with the PIV laser sheet by transmitting the PIV sheets through the final 283-nm turning mirror (see Fig. 1). The PIV and PLIF sheets were overlapped in the near and far fields and also in the probe region; this process was repeated daily, and the overlap was found to be very good each day. Sheet thicknesses were measured by translating a narrow slit through each beam and using a photodiode to record the spatial distribution; with this approach the 283 nm beam was determined to be ~400  $\mu$ m at the probe volume. The resulting fluorescence was acquired with a CMOS camera (LaVision HSS6) and external, two-stage, lens-coupled intensifier (LaVision HS-IRO). The intensifier uses a 25mm diameter S20 photocathode and P47 phosphor in the first stage, and S20T / P46 for the second (booster) stage. The camera has an array of 1024  $\times$  1024 pixels, each 20- $\mu$ m, that are digitized to 12-bit resolution. The camera operates in full-frame mode at up to 5400 frames per second (fps) and contains sufficient on-board memory (8 GB) for 5450 images or (as in this study) 1.09 s imaging time at 5 kHz. The lens-coupled intensifier is distinct from that used in our previous experiments in that it utilizes

custom-designed, built-in coupling optics with a significantly larger aperture and consequently less vignetting of the intensified image.

Fluorescence was collected with a fast Cerco 45mm,  $f/1.8$  lens which is AR coated for the UV. The lens was mounted to the external intensifier, and both intensifier and camera were mounted on a rail to more easily adjust the field of view, which was set to be  $\sim 86 \times 86$  mm, to view the entire width of the swirl burner (described below); as noted above, the 283-nm laser sheet covers only a portion of the height of the field of view. Background luminosity was reduced using a 500-ns intensifier gate. Elastic scattering at 283 nm was blocked using a high-transmission ( $> 80\%$  at 310 nm) bandpass interference filter (Custom fabrication - Laser-Components GmbH) and a colour glass filter (1 mm thick WG295). Flat-field correction for spatial variation of the laser sheet-intensity and other imaging nonuniformities was accomplished using a mean image derived from laser-induced fluorescence of acetone that was doped into the combustion chamber. Run-to-run background and camera noise was corrected using a 1000 frame ensemble average acquired while the lasers were blocked.

#### Particle Image Velocimetry System

The stereoscopic PIV system is based on a dual-cavity, diode-pumped, solid state Nd:YAG laser (Edgewave, IS-611DE) and a pair of CMOS cameras (LaVision HSS5). This laser produces 2.6 mJ/pulse at 532nm at a repetition rate up to 10 kHz. As the laser is pulse-energy (as opposed to quasi-cw average power) limited, this corresponds to 13 W per head at 5 kHz. Pulse duration is  $\approx 14$  ns. Pulse timing separation for the PIV system ranged from  $\Delta t = 20$  to 30  $\mu$ s, depending on the flow conditions, with the OH-PLIF excitation pulse temporally interlaced between the first and second PIV pulse of each measurement cycle. As with the PLIF system, three cylindrical lenses were used to form the sheet:  $f_{\text{piv1}} = -25$  mm,  $f_{\text{piv2}} = 300$ mm, and  $f_{\text{piv3}} = 1000$

mm. To minimize noise arising from inter-frame particle dropout, the beam waist was located somewhat beyond the probe region. The sheet thicknesses were measured in the same manner as for the PLIF beam; at the probe volume, the sheet thicknesses were  $\leq 0.7$  mm. Mie scattering from titanium dioxide ( $\text{TiO}_2$ ) particles seeded into the flow was imaged using a pair of CMOS cameras mounted equidistant from opposite sides of the laser sheet (see Fig. 1). Although the forward-scattering imaging configuration may result in different beam-steering effects for each camera, this is offset by the stronger and more uniform scattering intensity afforded by this approach. The HSS5 cameras are 10-bit,  $1024 \times 1024$  pixel imaging arrays ( $17 \mu\text{m}$  square pixels) and are capable of imaging at up to 3000 fps in full frame mode. Operated in two-frame PIV mode at 5 kHz, this array size is reduced to  $512 \times 512$  pixels. It is important to note that this reduced frame size is the result of partial readout of the image array and not from pixel-binning. Thus, SNR and resolution remain unchanged compared to full-frame operation. Each PIV camera has sufficient on-board memory (2.6 GB) for 4096 dual-frame images (i.e., 0.8 seconds imaging) at this resolution. For both PIV cameras, scattered light was collected with a Tokina 100-mm focal length lens with the f-stop set to f/5.6, and image-blur due to off-axis defocusing was corrected using a Scheimpflug adaptor between the lens and camera. The relatively short integration time ( $100 \mu\text{s}$ ) eliminated the need to use interference or coloured-glass filters. Perspective distortion was corrected using a dual-plane, three dimensional imaging target (LaVision Type 7). The same target was used to map the fields of view of the stereoscopic PIV and PLIF systems to one another. Image mapping, calibration, and particle cross-correlations were completed using a commercial, multi-pass adaptive window offset cross-correlation algorithm (LaVision DaVis 7.2). Final window size and overlap were  $16 \times 16$  pixels and 50%, respectively. This corresponds to a spatial resolution of 0.94 mm and vector spacing of 0.47 mm.



## Burners

To date, two burners have been studied with this system, the DLR Gas Turbine Model Combustor (GTMC) and a lifted turbulent non-premixed jet diffusion flame. As the GTMC has been extensively characterized and described elsewhere [15-17], only a brief description is presented here. The GTMC consists of two parts, the combustion chamber and the swirl burner. The combustion chamber has a square cross-section measuring 85 mm × 85 mm and stands 114 mm tall with walls of quartz plates, which allow the transmission of visible and UV radiation. The chamber is capped with a steel plate with a central exhaust tube (dia. 40 mm, length 50 mm) over a conical contraction. Air enters the combustion chamber through a central nozzle (diameter 15 mm) and a concentric annular nozzle (ID = 17 mm, OD = 25 mm contoured to OD = 40 mm). Both nozzles are fed from a common, upstream plenum. The air is swirled via a set of vanes upstream of each nozzle. Fuel is delivered through a ring of 72 channels (0.5 mm × 0.5 mm) positioned concentrically between the two air nozzles. The exit planes of the fuel and air nozzles stand 4.5 mm below the exit plane of the outer air nozzle, which we define as height  $h=0$ . In this burner only the air is seeded with particles. For the run condition presented in this paper, the burner consumed 281 g/min air and 12.3 g/min CH<sub>4</sub>, resulting in a thermal power of 10 kW and equivalence ratio of 0.75.

The jet diffusion flame burner consists of a 4 mm inner diameter tube, surrounded by a low-velocity co-flowing air stream. The co-flow is conditioned via a settling chamber followed by a bed of glass beads, wire mesh screen and finally a contoured nozzle to the exit plane. The first 110 mm downstream of the exit plane of the jet are surrounded by a rectangular duct of quartz plates, to block flow disturbances from the ambient environment and ensure uniform seeding of both the co-flow and jet at the flame base. The turbulent lifted jet flame was fueled with a

mixture containing 75% C<sub>3</sub>H<sub>8</sub> and 25% argon and had a jet-exit Reynolds number of 15,000 based on ambient temperature and pressure. Although cropped slightly in Figure 2 for better display, the OH-PLIF imaging region extended from approximately 65 to 125 mm downstream of the jet-exit. The overlapped stereo-PIV measurement region extended from approximately 65 to 95mm downstream. The flame base was observed to remain within the overlapped PIV-PLIF imaging region throughout each complete 0.8 s experiment run.

## **Results and Discussion**

Figure 2a shows a sample planar measurement of the lifted jet flame acquired with this system. As one can see, the region of overlap between the PIV and PLIF measurements is sufficient to capture both the higher velocity fluid along the jet centerline and the lower velocity fluid at the jet periphery and in the co-flow region. The overlap region is also sufficiently large to reliably capture the large-scale fluctuations in downstream location of the flame base throughout the entire 0.8 s measurement run.

Figure 2b shows a sample measurement of the swirl flame imaged in this study. The height of the OH-PLIF imaging region is comparable (approximately 40mm vs. 50mm) to that of Sadanandan et al. [18] and Stöhr et al. [19], who studied the same burner at 10Hz with over an order of magnitude more excitation energy (2.5 mJ / pulse), demonstrating the maturity level and technical relevance of the system described in this work.

The vectors shown in Figure 2a demonstrate an especially useful capability of the system. Recall, Upatnieks et al. [5] notes that the dynamic range of a high frame-rate PIV system may be significantly increased by cross-correlating images from temporally non-adjacent cycles (e.g., frames 0&2, 1&3, 2&4, etc). The vectors shown in Figure 2 constitute an extension of this

technique, wherein vector fields extracted from the cross-correlation of two frames of a given cycle are filtered based on a particle displacement threshold and combined with velocity vectors determined via the cross-correlation of the first frame of image-pairs in temporally adjacent cycles. Combining the user-specified inter-frame timing separation with the quasi-constant intercycle time of the PIV system provides a significant extension of the measurement dynamic range. In the present work, this allows us to accurately capture both the centerline velocity (including the major fluctuations induced by the passage of large-scale vortical structures) as well as the low-velocity region where the flamebase resides. This is a particularly important point for this flowfield: the range of velocities, from jet center to jet periphery, could otherwise exceed the PIV-instrument dynamic range.

Figure 3 shows every 5th frame of the measurement sequence from which the Figure 2a was extracted. An extended version of this measurement sequence containing every image (in the form of an avi video file) maybe found online at (publisher's website). In this sequence, beginning around 4ms we observe a large scale vortical structure rising up through the higher velocity jet-fluid. Consistent the observations of Boxx et al. [14], from 5ms onwards the flame is seen to distort and conform to the passage of this structure taking on what they describe as a 'fishhook type' shape. By 7ms, multiple discontinuities are observed in the OH-region, suggesting local extinction has occurred and by 9ms, these discontinuities have disappeared and a contiguous OH-zone at the flame base is reestablished. Consistent with the observations of Upatnieks et al. [5], the absolute downstream location of the flamebase is largely unaffected by the passage of this large-scale vortex structure. However, the effect of this structure on the OH-zone at the flame base is clearly significant. The vortex structure is linked to the formation of

multiple local discontinuities in the flame sheet at the base, which then heal as the vortex passes by.

Although the jet-exit Reynolds number of this flame is higher (15,000 vs. 8000) than that of their study, the penetration of high velocity fluid through the heat-release zone of the lifted flame and subsequent healing of the flame sheet stands in contrast with the work of Upatnieks et al. [5], who postulate that the lifted flame is stabilized via near-laminar propagation of an edge flame through a low-velocity region formed by local expansion of flow streamlines at the leading edge. This figure shows velocity fluctuations induced by the passage of large-scale vortical structures play a significant role in the turbulence-chemistry interaction at the base of a turbulent lifted jet flame. At least at the moderate Reynolds number studied in this work, such fluctuations are not uniformly dissipated by the presence of the flame and are occasionally strong enough to induce local extinction within the flamebase stabilization region.

Figure 4 shows a measurement sequence of the swirl flame. The corresponding movie is found at (publisher's website). In this figure, the regions without OH (white) represent gas at low and medium temperatures ( $T < 1500\text{K}$ ), e.g. fresh fuel/air mixtures. The dark regions (high OH levels) are burned gas at high temperature and the reaction zones are located at the transition from light to dark regions. Furthermore, OH is present in superequilibrium concentrations in the reaction zones, making the sharp increase of OH a good marker for the flamefront [18]. Near the flame axis, an (inner) recirculation zone can be seen transporting hot combustion products down to the nozzle exit. Within the inflow of fresh gas, a series of vortices shed periodically near the nozzle exit can be identified. Previous studies have shown conclusively that such vortices are part of a tornado-like precessing vortex (termed the precessing vortex core or PVC). In this sequence it is clear that the effect of this vortex is to mix the hot gases from the inner

recirculation zone with the cold incoming gases, thereby igniting the fresh gas and inducing a flamefront in the boundary layer between the fresh and burned gases. Subsequently the flame grows as it propagates and induces a heat release zone which grows as it passes from the field of view. Indeed the interplay of the PVC and the flamefront is a dominant feature of the turbulence-chemistry interaction. As before, the interaction of the heat-release region with the turbulent flowfield is clearly identifiable in these long-duration time resolved image sequences. Although the mean physical characteristics of the PVC and heat-release zones observable in this sequence have already been well characterized in previous work, these measurements illustrate the temporal development of the vortex-flame interaction and immediately allow the determination of the frequency of periodic instabilities.

In summary we describe an approach of imaging the interaction of the flamefront, using OH PLIF, and flowfield, using stereoscopic PIV, at 5 kHz. The utility of this diagnostic is demonstrated in a lifted jet flame and in a flame with swirl. In both cases the dynamics of the flame stabilization processes are seen. Clearly, non-periodic effects such as local ignition and/or extinction, lift-off and flashback events and their histories can be captured by this technique. As such, this system has the potential to significantly extend our understanding of nonstationary combustion processes relevant to industrial and technical applications.

## **Acknowledgements**

C. Carter acknowledges support of the Air Force Office of Scientific Research Windows on Europe Program.

## References

1. Raffel, M. Willert, C., Wereley, S. T., and Kompenhans, J., *Particle Image Velocimetry: A Practical Guide*, Springer, Berlin (2007).
2. Frank, J. H., Lyons, K. M., and Long, M. B, *Combust. Flame* **107**, 1 (1996).
3. Hasselbrink, E.F., Mungal, M.G., and Hanson, R.K., “Planar velocity measurements and OH imaging in a transverse jet flame,” AIAA Meeting Paper AIAA 97-0118, Reno, NV, 1997.
4. Fajardo, C.M., Smith, J. D., and Sick, V., *Appl. Phys B* **85**, 25 (2006).
5. Upatnieks, A., Driscoll, J. F., Rasmussen, C. C., and Ceccio, S. L., *Combust. Flame* **138**, 259 (2004).
6. Steinberg, A. M., Driscoll, J. F., and Ceccio, S. L., *Exp. Fluids* **44**, 985 2008.
7. Kaminski C.F., Hult, J. and Alden, M., *Appl. Phys. B* 68, 757 (1999)
8. Olofsson, J., *Laser Diagnostic Techniques with Ultra-High Repetition Rate for Studies in Combustion Environments*, Doctoral Dissertation, Lund University, Division of Combustion Physics, Lund, Sweden (2007).
9. Jiang, N., and Lempert, W., *Opt. Lett.* **19**, 1, 2008.
10. Miller, J. D., Slipchenko, M., Meyer, T. R., Jiang, N., Lempert, and Gord, J. R., *Opt. Lett.*, in press.
11. Paa, W., Muller, D., Stafast, H., and Triebel, W., *Appl. Phys. B* **86**, 1 (2007).
12. J. Wäsle, A. Winkler, T. Sattelmayer, *Flow, Turbulence and Combustion* 2005 75: 29–50.
13. Kittler, C., and Dreizler, A., *Appl. Phys B* **89**, 163 (2007).

14. Boxx, I., Heeger, C., Gordon, R., Böhm, B., Aigner, M., Dreizler, A., Meier, W., *Proc. Combust. Inst.*, in press.
15. Boxx, I., Heeger, C., Gordon, R., Böhm, B., Dreizler, A., Meier, W., *Combust. Flame*, in press.
16. Weigand, P., Meier, W., Duan, X.R., Stricker, W., and Aigner, M., *Combust. Flame* **144**, 205 (2006).
17. Meier, W., Duan, X.R., and Weigand, P., *Combust. Flame* **144**, 225 (2006)
18. Sadanandan, R., Stöhr, M., Meier, W., *Appl. Phys. B* **90**, 609 (2008).
19. Stöhr, M., Sadanandan, R., Meier, W., *Proc. Combust. Inst.*, in press.

### **List of Figures:**

Figure 1 – a) Diagnostics and burner experiment Setup b) DLR Gas Turbine Model Combustion (reproduced from Stöhr et al. [19])

Figure 2 – OH-PLIF / PIV Image of the a) lifted flamebase and b) Swirl Flame, showing region of overlap between OH-PLIF and Stereoscopic PIV systems.

Figure 3 – Measurement sequence (every fifth frame) showing the deformation and local extinguishment of the flame sheet by a large scale vortical structure. The flame sheet quickly re-establishes itself in the low-velocity region after the vortex passes by, suggesting the flame location is significantly effected by turbulent phenomena in the flow-field.

Figure 4 – Measurement sequence showing the effect of the precessing vortex core on the mixing of hot gases from the interior recirculation zone with the incoming gases.



## Figures

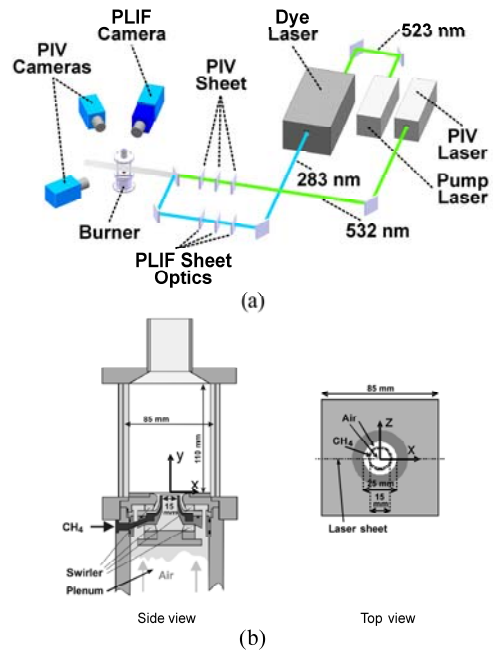


Figure 1

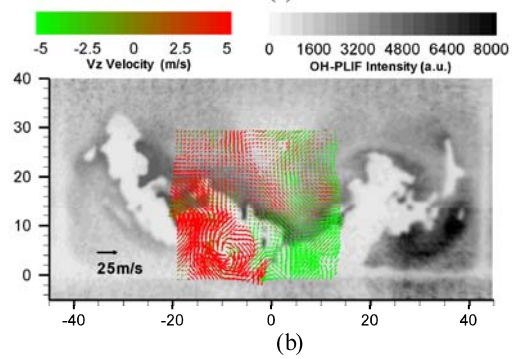
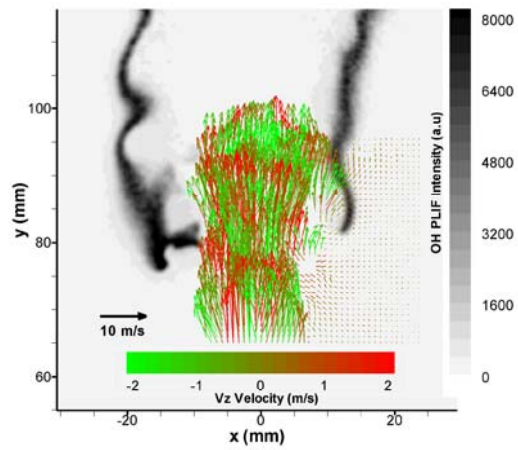


Figure 2

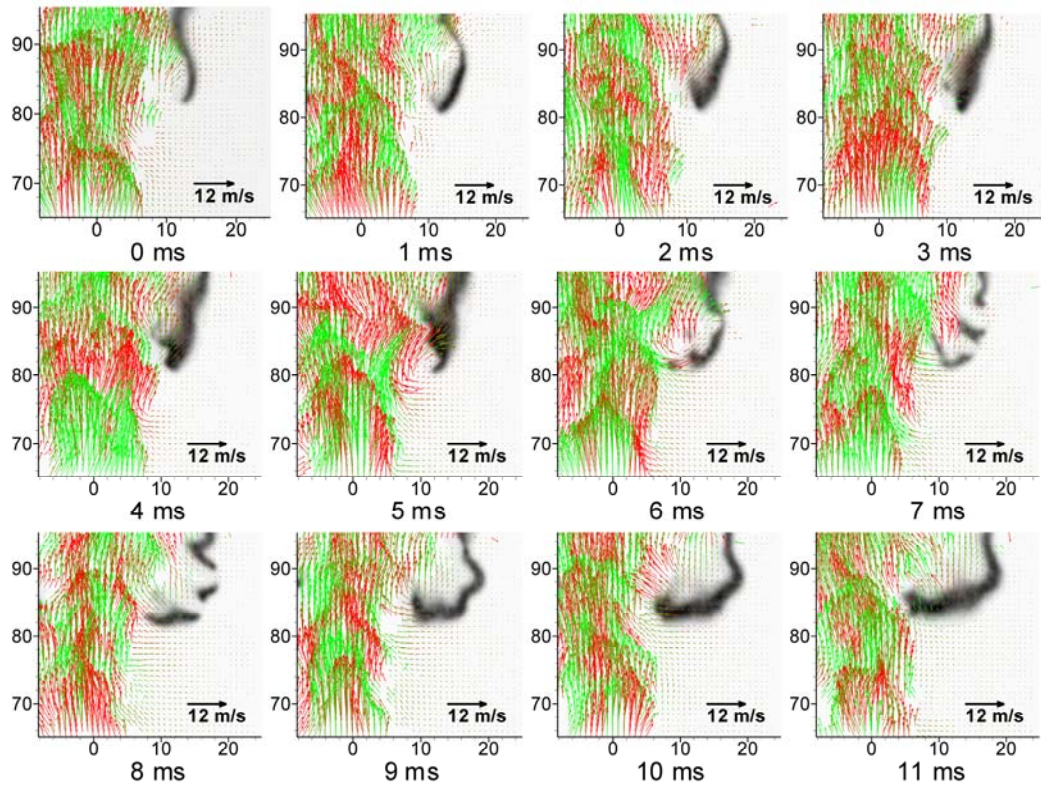


Figure 3

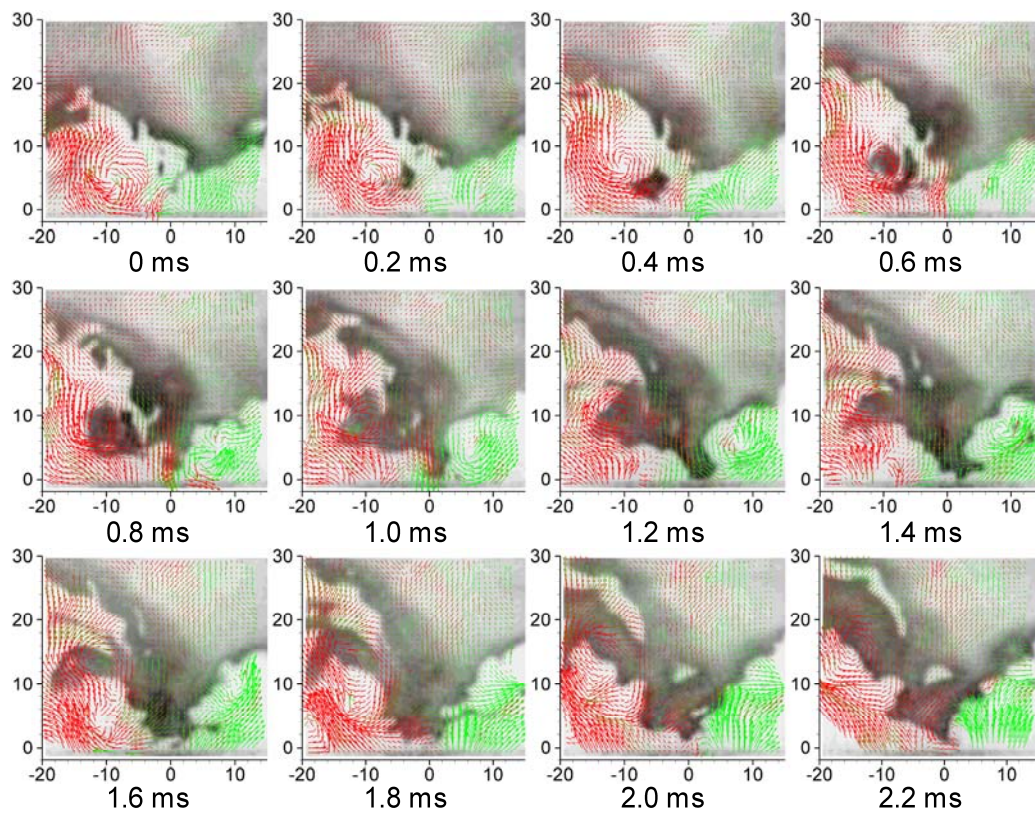


Figure 4